The Nocturnal Surface Inversion and Influence of Clear-Air Radiative Cooling

J. C. ANDRÉ[1] AND L. MAHRT

Department of Atmospheric Sciences, Oregon State University, Corvallis 97331

(Manuscript received 30 March 1981, in final form 10 December 1981)

ABSTRACT

Nocturnal boundary-layer data from the Wangara and Voves experiments are analyzed. The lower part of the nocturnal inversion layer normally appears to be turbulent but strongly stratified. The upper thicker part of the inversion layer is characterized by weaker stratification which appears to be almost completely generated by clear-air radiative cooling. The radiative cooling is associated primarily with moisture, but is only modestly sensitive to the particular moisture distribution and thus varies little from night to night for the data analyzed here.

The radiatively cooled layer thickens significantly as the night proceeds. On the other hand, the thickness of the turbulent layer normally varies slowly during the night, but differs significantly from night to night. For the inversion layer as a whole, turbulent heat flux divergence and clear-air radiative cooling make comparable contributions to the heat budget.

The stratification normally decreases with height corresponding to negative curvature of the potential temperature profile. However, with increasing relative importance of the turbulence, this negative curvature weakens and may even become positive as with nearly well-mixed flow.

1. Introduction

During clear nights over land, one can usually observe the progressive build up of a stably stratified layer next to the surface. This layer will be referred to as the nocturnal surface inversion (NSI) or inversion layer. The turbulent nocturnal boundary layer (NBL) normally occupies only the lower part of the inversion layer. Development of the surface inversion layer is thought to be due to three main processes. Firstly, any shear-generated turbulence leads to downward heat flux to the cooled surface and corresponding upward extension of the cooling. Secondly, clear-air radiative cooling due to emission by water vapor, carbon dioxide, ozone and aerosols can stratify low-level air. Finally, horizontal advection, particularly over sloped terrain, can modify the local depth of the inversion layer (Ball, 1956).

Most previous studies have attempted to explain the development of the nocturnal boundary layer in terms of only turbulent heat transfer to the cooled surface (e.g., Delage, 1974; Wyngaard, 1975; Brost and Wyngaard, 1978; Zeman, 1979) or have examined the surface inversion layer in terms of only clear-air radiative cooling (e.g., Brunt, 1934; Anfossi *et al.*, 1976; Klöppel *et al.*, 1978). A few studies of the nocturnal surface inversion have considered simultaneously both turbulent and radiative heat transfer (André *et al.*, 1978, Yamada, 1979, Nieuwstadt, 1980). Unfortunately, observational verification of models of either the nocturnal boundary layer or the surface inversion layer remains tentative and rather indirect. In particular, the very few direct measurements of radiative flux divergence have been confined to layers much thinner than the depth of the boundary layer. Furthermore, the weak and intermittent fluxes in the nocturnal boundary layer may require a prohibitively long averaging time.

The intent of this study is to present observational evidence for the interaction between turbulent transport and clear-air radiative cooling in the development of the nocturnal surface inversion. We shall primarily analyze data collected over a relatively flat and treeless plain in southeastern Australia during the Wangara experiment (Clarke *et al.*, 1971) and data collected over grain fields of the Beauce plain south of Paris during the Voves experiment[2] (e.g., André and Lacarrère, 1980). For the sake of simplicity we shall restrict most of our study to clear sky conditions, but will also show a few results for conditions which are synoptically active or cloudy. While these data sets are somewhat incomplete for present purposes, they do provide useful information on aspects of the nocturnal surface inversion which thus far have been considered only from a modeling point of view.

[1] On leave from Direction de la Météorologie (EERM/GMD), Boulogne, France.

[2] Data collected during the Voves experiment can be found in several catalogs edited by A. Weill at "Centre de Recherches en Physique de l'Environnement" (38 rue du Général Leclerc, 92131 Issy les Moulineaux, France).

0022-4928/82/040864-15$07.75

2. Data

A night is classified as clear if the low-level cloudiness is less than one octa, the total cloudiness is less than two octas and the surface net radiative flux is upward with a magnitude greater than 6 W m^{-2}. For Wangara these criteria are satisfied by 10 nights beginning on days 7, 11, 12, 13, 18, 30, 31, 32, 33 and 42. For the Voves experiment, these criteria are satisfied for nights beginning on July 1, 2, 5, 6, 7, 10 and 14, of 1977. For most of the above 17 nights, soundings of wind, temperature, and specific humidity are available at more or less equally-spaced time intervals between sunset and sunrise.

Radiative fluxes and corresponding cooling rates are computed from a numerical model using profiles of temperature and specific humidity. It is similar to that used by André *et al.* (1978) and is described further in the Appendix. In the Appendix it is also shown that this model produces results in close agreement with those of a more precise model using detailed spectral resolution.

For the Voves experiment, we use surface heat fluxes deduced from the surface energy budget measurements by the method in Perrier *et al.* (1975). For the Wangara experiment, we use values of the turbulent surface kinematic heat flux $Q_0 = (\overline{w'T'})_0$ estimated by Hicks (1976) from the profile-flux relationship presented in Webb (1970).

3. Various depth scales

Compared to the daytime convective boundary layer, the depth of both the NBL and the NSI are much more difficult to define and estimate from data. A variety of definitions for both the NBL and NSI can be constructed, based on different physical properties and methods of computation from data. For a given nocturnal situation, these different estimates can vary by several factors.

The inversion layer is usually defined as either the height h_θ to which significant cooling has extended (e.g. Melgarejo and Deardorff, 1974) or h_i, the depth of the stably stratified layer (Yu, 1978). The depth of the cooling, h_θ is constructed by differencing consecutive temperature soundings which may lead to considerable noise. The inversion height h_i, proposed by Yu (1978) is specified to be the altitude where the temperature gradient $\partial\bar{T}/\partial z$ vanishes. This specification excludes the upper part of the cooled layer where the stratification is weaker, but significantly larger than in the overlying air. We modify Yu's definition of the inversion layer to include the thicker layer adjacent to the surface where the potential temperature gradient $\partial\bar{\theta}/\partial z$ exceeds 3.5×10^{-3} K m^{-1}, the low-level value of the standard atmosphere (e.g., Cole *et al.*, 1965). Any definition of the top of the inversion layer may appear somewhat arbitrary since

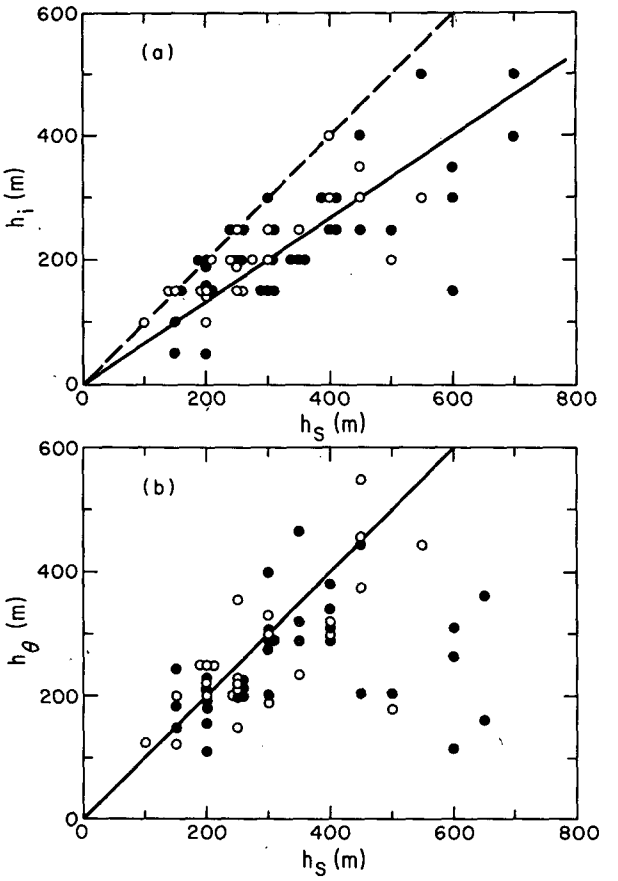

FIG. 1. Scatter diagram showing: (a) Yu's (1978) inversion height h_i versus inversion depth h_s (the solid line is $h_s = 1.5\ h_i$); (b) Melgarejo and Deardorff's (1974) cooling depth h_θ versus inversion depth h_s. Filled circles correspond to "selected" data used in the present study while open circles represent the remaining Wangara data.

radiative cooling sometimes occurs throughout the entire troposphere and differential advection can lead to stratification greater than that of the standard atmosphere. However, in 75% of our cases the vertical transition between the inversion layer and the overlying almost-neutral layer is sufficiently sharp that the computed top of the inversion is not sensitive to modest changes in the stratification cut-off value. In most of the remaining cases, the transition is quite smooth with no overlying near-neutral layer. Our definition of the depth of the surface inversion h_s is on the average ~50% larger than the depths h_i estimated by Yu and comparable to the cooling depths h_θ estimated by Melgarejo and Deardorff (see example in Figs. 1a and 1b). These three estimates of the surface inversion depth are listed in Table 1 for the subset of Wangara profiles previously selected by Melgarejo and Deardorff (1974).

The depth of the turbulent boundary layer or NBL is much more difficult to assess from observations. In stable conditions, the turbulence can be weak and

TABLE 1. Wangara inversion depths. Values of h_θ are based on Melgarejo and Deardorff (1974); values of h_i are based on Yu (1978).

Day	Hour	h_θ (m)	h_i (m)	h_s (m)
1	6	190	200	300
	18	200	150	150
	21	220	250	250
	24	355	200	250
4	3	445	300	550
	6	455	300	450
6	18	125	100	100
	21	200	150	200
7	3	300	250	300
	6	235	250	350
	18	180	200	200
	21	320	200	350
	24	295	150	300
10	24	210	150	250
11	24	290	150	300
12	6	265	300	600
	21	465	200	350
	24	275	250	300
13	3	160	500	650
	6	360	400	650
	18	230	150	200
	21	195	200	250
	24	205	250	500
14	3	115	150	600
	6	310	350	600
	21	180	200	500
	24	320	300	400
16	24	150	150	250
18	24	155	50	200
19	3	200	200	300
	6	205	250	450
25	21	250	150	200
26	6	220	200	200
	21	250	150	200
30	21	200	200	250
	24	340	300	400
31	3	320	250	400
	6	290	250	400
	21	195	200	200
	24	110	150	200
32	3	390	200	350
	6	380	300	400
	24	150	150	150
33	3	305	300	300
	18	245	50	150
	21	185	100	150
	24	400	150	300
34	3	450	400	450
	6	650	500	550
	18	250	100	200
	21	225	200	250
35	6	395	400	400
39	3	375	350	450
	24	200	200	250
40	3	125	150	150
42	21	215	250	250
	24	205	200	200
43	3	225	250	250
44	3	330	—	300
	6	550	—	450

intermittent and may exist in more than one distinct layer (e.g., Ottersten *et al.*, 1973). Thus, estimates of the depth of the turbulence are sometimes ambiguous. For example, our efforts to determine the depth of the NBL using acoustic sounder data from the Voves experiment often yielded ambiguous results. Moulsley *et al.* (1981) also found interpretation of acoustic sounder records to be difficult. The height of the low-level wind maximum cannot be used since it is often influenced significantly by baroclinity and nonstationarity of mean flow and sometimes does not exist.

In this study we estimate the depth of the turbulence from profiles of the Richardson number computed over layers of ~50 m thickness. These computed profiles most often show small values in a layer adjacent to the surface and very large values in the immediate overlying region, as in the composited profiles presented in Mahrt *et al.* (1979). Consequently, the implied depth of the turbulence h_R can be estimated to be the height where the Richardson number first exceeds a threshold value without the computed depth h_R becoming too sensitive to the particular numerical choice of threshold value. Here we use 0.5 as a threshold value, this value being typical of the critical Richardson numbers cited in papers surveyed by Mahrt (1981). Varying this threshold value by a factor of two, for example, does not change the results significantly because of the steep gradient of Richardson number at the top of the turbulent layer.

Another possibility would be to estimate the depth of the turbulence from the profile of the momentum flux determined by applying the residual technique to the momentum budget, neglecting advections and evaluating other terms from consecutive wind soundings. However, our analysis indicated that errors in various terms in the momentum budget were likely to be too large to allow for estimation of profiles of the eddy-flux divergence. Uncertainty in the geostrophic wind may be particularly large.

The effect of errors in the geostrophic wind value can normally be reduced by differentiating the momentum budget with respect to height, in which case we obtain

$$\frac{\partial}{\partial t}\frac{\partial}{\partial z}\mathbf{V} = -2\boldsymbol{\Omega} \times \frac{\partial}{\partial z}\mathbf{V}_{ag} - \frac{\partial^2}{\partial z^2}\overline{w'\mathbf{V}'}, \qquad (1)$$

where $\mathbf{V}_{ag}$ is the ageostrophic wind and other variables have the usual notation. Here we assume barotropic flow in which case knowledge of the geostrophic wind is not needed. We estimate profiles of the stress curvature by evaluating the other two terms from measured wind profiles. The estimated stress curvature decreases very rapidly with height and then quickly reaches a slowly varying small

value, allowing for a relatively easy estimation of a depth scale h_{sh}. This depth scale shows the same nocturnal evolution as the depth h_R computed from the Richardson number profile on the three nights (Wangara 18–19, 30–31, 42–43) when h_R varied significantly with time (Table 2). However, these depths h_{sh} based on the shear equation are larger than h_R by an amount that varies substantially from night to night.

The large differences between various depths are evident in Table 2 and in the individual selected profiles shown in Fig. 2. These differences underscore the requirement that the physical definition of the depths and possible method of estimation from observations must be carefully detailed before modeling is attempted. Note that the estimated thickness of the turbulence is roughly only one third of that of the inversion layer. This may partially explain why models based on surface turbulent fluxes account for only a small portion of the variance of the observed depths of the inversion layer and momentum boundary layer (Yu, 1978).

Above the nonturbulent, radiatively-cooled layer, the flow may also become turbulent. On 23 of the 39 Wangara soundings listed in Table 2, the Richardson number decreases to values <0.5 within 100 m above the top of the inversion layer h_s. In all but two cases the Richardson number decreases to values <0.5 within 500 m above h_s and always below the top of the previous day's mixed-layer top, when definable. The small Richardson numbers and possible turbulence above the inversion layer are associated with weak stratification, probably remnants from convective mixing on the previous day, and associated with shear occurring on the upper side of the low-level wind maximum. Intermittent turbulence also appears above the nocturnal surface inversion in the numerical modeling of André *et al.* (1978). When present, this turbulence could contribute to further growth of the inversion layer. These turbulent layers above the nocturnal surface inversion could be viewed as entraining into the nonturbulent upper part of the inversion layer.

The time-evolution of the depths of the various layers are quite different (Fig. 3). The depth of the turbulent NBL varies slowly with time while the depth of the surface inversion increases more rapidly, especially after midnight. The thickening of the inversion layer can be attributed to clear-air radiative cooling as is discussed further in Sections 4 and 5.

TABLE 2. Depths of the inversion layer and turbulent- and shear-boundary layers for the selected clear nights during the Wangara and Voves experiments.

Day	Hour	h_R (m)	h_s (m)	h_{sh} (m)
		Wangara		
7	21	30	350	100
8	00	35	300	80
	03	35	400	75
	06	50	200	
11	21	70	250	150
12	00	115	300	160
	06	60	600	
	21	60	350	120
13	00	60	300	130
	03	40	650	200
	06	35	650	
	21	35	250	100
14	00	40	500	190
	03	30	600	200
	06	140	600	
18	21	90	150	190
19	00	60	200	150
	03	35	300	100
	06	30	450	
30	21	115	250	160
31	00	140	400	190
	03	170	400	215
	06	65	400	
	21	40	200	110
32	00	40	200	110
	03	35	350	120
	06	45	400	
	21	35	200	100
33	00	30	150	90
	03	30	300	90
	06	40	300	
	21	75	150	200
34	00	45	300	300
	03	55	450	250
	06	50	550	
42	21	30	250	100
43	00	35	200	140
	03	75	250	170
	06	125	700	
		Voves		
2	04	40	400	
	19	65	100	
3	04	85	350	
	07	—	300	
6	04	50	250	
7	00	100	250	
	06	—	350	
8	04	220	400	
10	21	85	150	
11	00	80	300	
	02	250	300	
	05	120	350	
15	05	210	350	

4. Inversion layer heat budget

The sensible heat budget can be written as

$$\frac{\partial \bar{T}}{\partial t} = \frac{-\partial}{\partial z}\overline{w'T'} - \frac{1}{\rho C_p}\frac{\partial F}{\partial z} + A, \qquad (2)$$

where $\bar{T}$ is the mean temperature, ρ the density, C_p the specific heat capacity, F the net long-wave radiative flux and A the residual due to temperature

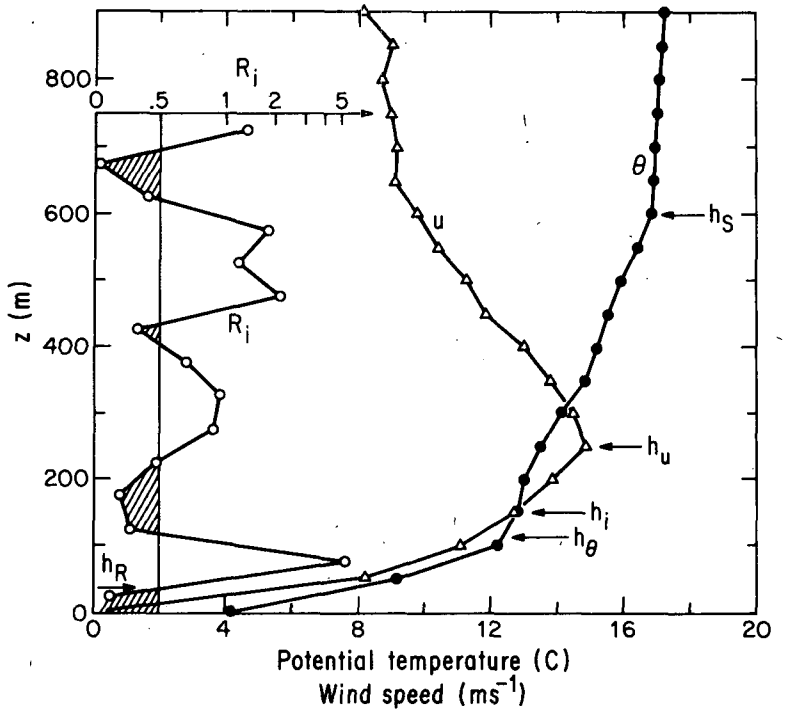

FIG. 2. Various depths of the nocturnal boundary layer for Wangara Day 14 at 0300 LST.

advection and various errors in the estimation of the other terms.

Integrating (2) from the surface to any height h, greater or equal to the depth of the turbulence h_R, we obtain

$$C \equiv \int_0^h \frac{\partial \bar{T}}{\partial t}\, dz = Q_0 + \Delta F + I, \tag{3}$$

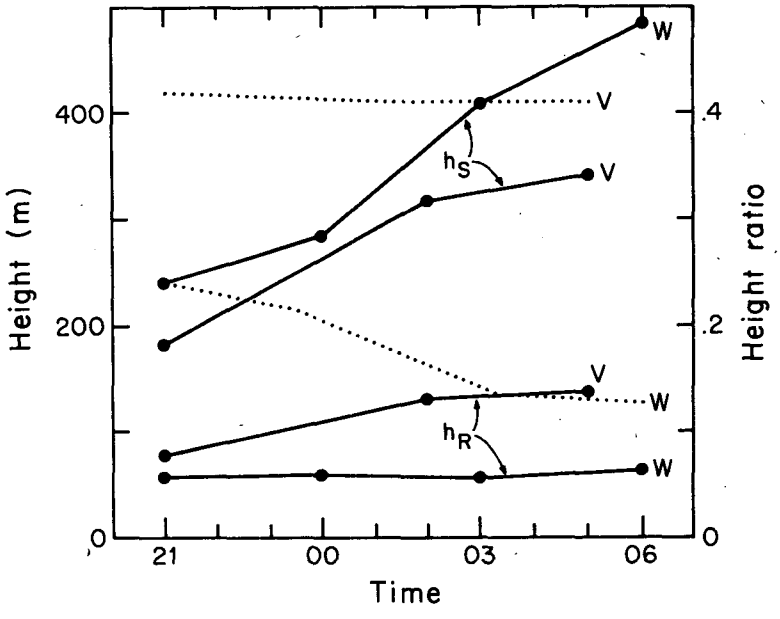

FIG. 3. Evolution of the depths of the turbulent NBL (h_R) and of the stable surface inversion (h_s) for Wangara (W) and Voves (V.) experiments. The ratios h_R/h_s are indicated with dotted lines.

where:

$$Q_0 \equiv (\overline{w'T'})_0,$$

$$\Delta F \equiv \frac{1}{\rho C_p}[F(0) - F(h)],$$

$$I \equiv \int_0^h A dz,$$

and the subscript 0 refers to surface properties.

The vertically-integrated budget (3), averaged over all of the observations, is presented in Table 3a for the entire inversion layer of depth h_s. The integrated temperature change C is computed by subtracting two consecutive soundings while the hourly surface turbulent heat fluxes given by Hicks (1976) are averaged over the inclusive time period between the two soundings to compute Q_0. The radiative term ΔF is estimated by vertically integrating the radiative flux divergence $\partial F/\partial z$ computed from temperature and humidity profiles according to Eq. (A1). The results are then averaged over the number of profiles available during the considered time interval. When required for any of the above calculations, linear interpolation between observational levels is used.

Note that for both Wangara and Voves, turbulent and clear-air radiative cooling each account for ~40% of the observed cooling while ~20% of the cooling remains unexplained residual (Table 3a). However, the heat budget varies significantly between individual cases as is reflected by the large standard deviations. On some nights clear-air radiative cooling dominates the heat budget for the inversion layer. For example, on Wangara night 11–12, clear-air radiative cooling accounts for 64% of the observed cooling compared to 21% explained by the turbulent heat flux. For some of the cases, the residual may be quite large and of either sign which leads to the large standard deviation shown in Table 3a.

The large budget residuals for individual nights are partly due to a relatively weak correlation between observed cooling and estimated surface heat fluxes. Surface heat fluxes, derived by Melgarejo and Deardorff (1975) using the profile inversion method based on Monin-Obukhov similarity, show similar weak correlation with the observed cooling and average ~35% smaller than those provided by Hicks (1976). This would nearly double the residual of the mean heat budget of Table 3a.

TABLE 3a. Averaged heat budget over the depth h_s of the inversion layer (10^{-2} K m s^{-1}). Standard deviations are set in italics.

	C	Q_0	ΔF	I
Wangara	−3.56	−1.38	−1.35	−0.83
		(39%)	(38%)	(23%)
	2.18	*1.01*	*0.48*	*2.14*
Voves	−3.34	−1.56	−1.19	−0.59
		(47%)	(36%)	(17%)
	0.71	*0.40*	*0.29*	*0.86*

TABLE 3b. Averaged height-dependent cooling budget over the depth h_s of the inversion layer (10^{-2} K m s^{-1}). Standard deviations are set in italics.

	C'	Q_0	$\Delta F'$	I'
Wangara	−3.18	−1.52	−0.36	−1.30
		(48%)	(11%)	(41%)
	1.25	*1.01*	*0.20*	*1.37*
Voves	−2.96	−1.72	−0.29	−0.95
		(58%)	(10%)	(32%)
	0.81	*0.40*	*0.14*	*0.89*

The surface heat flux estimated for Wangara from the observed net radiative flux at the surface less the heat flux from the soil (Clarke *et al.*, 1971) leads to heat fluxes which, on the average, are roughly 75% larger than those computed by Hicks (1976). Hicks attributed the difference between his surface fluxes and the surface radiative flux, less soil heat flux, to be due to surface latent heat flux resulting from dew formation or evaporation. We found only weak correlation between his inferred latent heat flux and the boundary-layer moisture budget. This is possibly due to the fact that the heat budget neglects soil heat storage between the thermistor level and the soil surface, and that the moisture budget neglects horizontal advection. With any of the above estimates, the uncertainty in the surface heat flux is likely to be large. The relatively small residual in the mean heat budget could be due to randomness in the errors of the turbulent heat flux and other terms.

Some of the observed cooling is independent of height and does not contribute to the development of the stable stratification of the inversion layer. Therefore, we have also computed the height dependent portion of the heat budget; that is the part which leads to the development of stratification. This budget excludes the height-independent cooling which extends above the inversion layer. The corresponding integrated cooling C' is computed as

$$C' = \int_0^{h_s} [\bar{\theta}(z) - \bar{\theta}(h_s)]dz/\tau,$$

where $\bar{\theta}$ is the potential temperature and τ is the time after radiative sunset taken as 1700 LST for Wangara and 1800 LST for Voves. The corresponding height-dependent integrated radiative cooling rate $\Delta F'$ becomes

$$\Delta F' \equiv \Delta F - \frac{h_s}{\rho C_p}\frac{\partial F}{\partial z}(h_s).$$

The turbulent cooling does not have to be modified since it is expected to vanish at h_s.

TABLE 4a. Averaged heat budget over the depth h_R of the turbulent NBL (10^{-2} K m s^{-1}). Standard deviations are set in italics.

	C	Q_0	ΔF	I
Wangara	−1.08	−1.38	−0.25	+0.55
		(128%)	(23%)	(−51%)
	0.84	*1.01*	*0.15*	*1.27*
Voves	−2.41	−1.74	−0.58	−0.09
		(72%)	(24%)	(4%)
	1.04	*0.36*	*0.32*	*1.04*

Results of this height-dependent part of the heat budget are shown in Table 3b. Once again, Wangara and Voves data lead to comparable estimates. However, now almost ⅓ of this budget remains unexplained residual, possibly due to an unrealistically small contribution from clear-air radiation (see Appendix for further discussion).

Due to scarcity of required data, it is not possible to determine detailed vertical structure of the heat budget. Instead, we obtain some information on vertical structure by integrating the heat budget over the turbulent layer h_R (Tables 4a and 4b) and comparing the results with the above heat budget for the entire inversion layer (Tables 3a and 3b). Note that in the turbulent NBL, clear-air radiative cooling is much less important than turbulent heat flux divergence, especially in the height-dependent part of the budget. While the cooling above the turbulent boundary layer is assumed to be due to radiative cooling, the role of intermittent turbulence and changes in depth of the turbulence cannot be ruled out.

Examination of the standard deviations indicates that the magnitude of the computed clear-air radiative cooling ΔF varies less from night to night than the observed surface heat flux Q_0. In particular, the computed radiative cooling rate is only moderately sensitive to the variations of vertical structure of temperature and moisture observed in Wangara and Voves.

To illustrate this further, the radiation model was run for various idealized profiles of moisture and potential temperature (Fig. 4). For a given thermal structure, the radiative cooling decreases by only ~15%, when the moisture value varies from 12 to 5 g kg^{-1}. This decrease reaches 30% when the moisture value varies from 12 to 1 g kg^{-1}. This relatively small sensitivity of radiative cooling to humidity changes is due to near-saturation of dependencies on moisture occurring in the absorptivity function of water vapor (see Appendix for more details).

Although the radiative cooling profiles show some dependence on temperature structure (Fig. 4), all profiles show maximum cooling near the top of the inversion layer and significant cooling above the inversion. This acts to thicken the inversion layer and probably explains why the inversion layer thickens with time during the night and why it is almost always at least 50% thicker than the turbulent layer (Table 2 and Fig. 3).

With increased stratification (Fig. 4), the cooling near the top of the inversion layer is further enhanced, while near the surface cooling is reduced or local warming appears. That is, air near the top of the inversion undergoes heat loss due to radiative exchange with the overlying atmosphere, colder un-

TABLE 4b. Averaged height-dependent cooling budget over the depth h_R of the turbulent-NBL (10^{-2} K m s^{-1}). Standard deviations are set in italics.

	C'	Q_0	$\Delta F'$	I'
Wangara	−1.33	−1.52	−0.03	+0.22
		(114%)	(2%)	(−16%)
	0.59	*1.01*	*0.02*	*1.15*
Voves	−1.83	−1.82	−0.10	+0.09
		(99%)	(6%)	(−5%)
	1.33	*0.45*	*0.09*	*1.56*

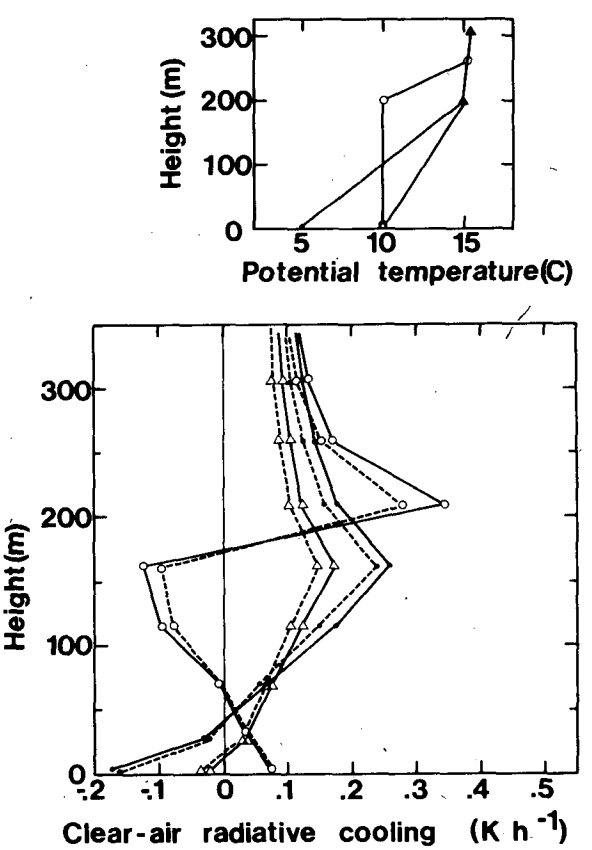

FIG. 4. Bottom: Profiles of clear-air radiative cooling rates for constant boundary-layer specific humidity (solid line, 12 g kg^{-1}; dashed line, 5 g kg^{-1}). Top: Corresponding potential temperature profiles. Filled circles, strong stratification; open triangles, weak stratification; open circles, mixed layer.

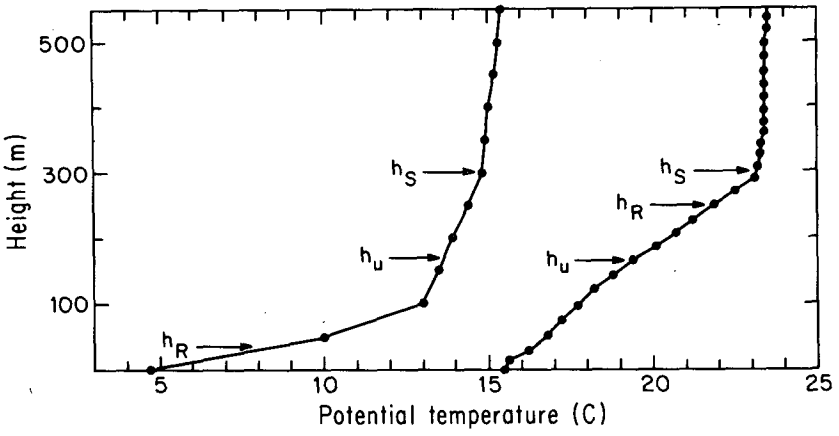

FIG. 5. Potential temperature profiles for Wangara Day 8 at 0020 LST (left) and for Voves 11 July at 0226 LST (right). Arrows indicate the respective heights of the surface inversion (h_s), low-level wind maximum (h_u) and turbulent boundary layer (h_R).

derlying air and the ground. On the other hand, air in the lower part of the inversion gains some heat due to radiative exchange with overlying warmer air since the absolute temperature increases with height throughout much of the inversion layer. Consequently, the profile of clear-air radiative cooling acts to thicken the inversion layer, but also acts to reduce the stratification within the inversion layer. Since the inversion layer is growing, the radiative cooling profile is nonstationary and does not lead to complete destabilization of the inversion layer. In contrast, turbulent heat fluxes act to increase the stratification in the lower part of the inversion layer through strong cooling near the surface. The influence of turbulence and clear-air radiation on temperature structure is discussed further in Section 5.

For comparison, Fig. 4 also shows radiative cooling profiles for the asymptotic case of well-mixed flow. Here significant radiative warming occurs in the bulk of the mixed-layer and fairly large radiative cooling occurs at the mixed-layer capping inversion and above.

The general picture emerging from the above considerations extends those of previous studies summarized by Paltridge and Platt (1976). These earlier studies were essentially restricted to the much thinner turbulent surface layer where radiative warming normally occurs in the first few centimeters above the ground (Coantic and Seguin, 1971; Kondo, 1971; Schaller, 1977) above which radiative cooling decreases rapidly from a few degrees per hour around 1 m to $\sim$1 K h^{-1} at 10 m (Funk, 1960; Elliott, 1964; Coantic and Seguin, 1971; Kondo, 1971; Schaller, 1977). The model examples provided by Elliott (1964) and Kondo (1971) mention values decreasing to the order of 0.1–0.2 K h^{-1}, at $\sim$100 m, in fairly good agreement with Figs. 4 and A1 (Appendix). The very thin layer of radiative warming should not normally contribute significantly to the bulk heat budgets of either the turbulent or inversion layers.

5. Vertical temperature structure

The previous section suggests that turbulent heat flux divergence dominates the cooling in the lower part of the inversion layer while clear-air radiative cooling accounts for extension of the inversion above the turbulent layer. Consequently we now study the behavior of the vertical distribution of potential temperature.

To illustrate variation of temperature structure, Fig. 5 shows an almost linear profile of potential temperature measured during the Voves experiment (0226 LST, 11 July) and a profile with strong curvature measured during the Wangara experiment (0036 LST day 12). A convenient way of quantifying such profile structure is to introduce the overall scaled curvature of the potential temperature profile defined as

$$\gamma = \frac{\bar{\theta}(h_s) - 2\bar{\theta}(h_{s/2}) + \bar{\theta}(0)}{\bar{\theta}(h_s) - \bar{\theta}(0)}. \qquad (4)$$

In the above examples (Fig. 5), the Wangara profile has a scaled curvature of -0.74, while the Voves profile has a scaled curvature of $+0.07$.

In the Voves case, the turbulent layer is relatively deep while in the Wangara case, the turbulent layer is thin and most of the inversion layer appears to be generated by clear-air radiative cooling. We can therefore postulate that strong negative curvature is most likely to be associated with cases where the bulk of the inversion layer is dominated by clear-air radiative cooling. Brunt (1934) theoretically showed that infrared radiative transfer behaves like a diffusive process leading to an exponential type temperature profile with strong negative curvature (see

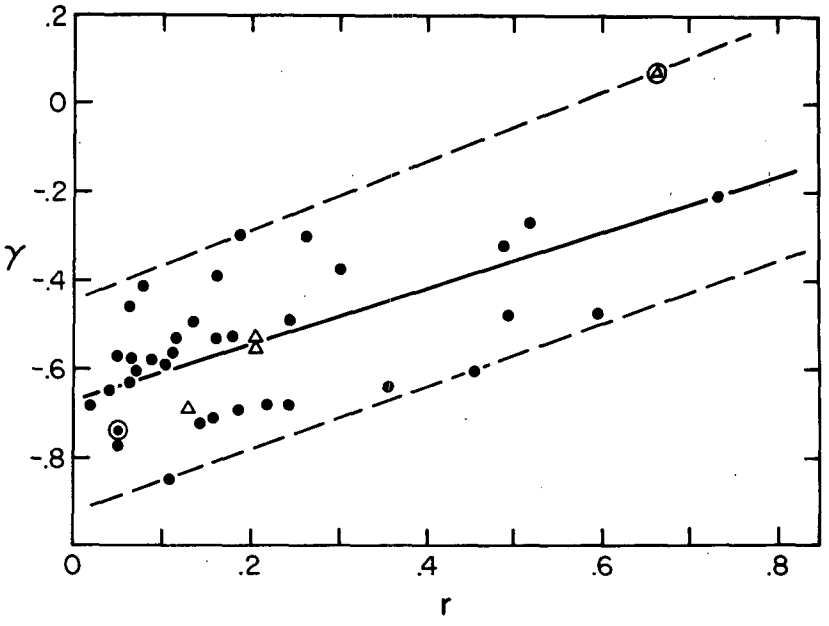

FIG. 6. Scaled curvature of the potential temperature profile γ, versus the ratio r of the radiative to the turbulent cooling rates. Filled circles, Wangara; and open triangles, Voves; circled points correspond to the two cases shown in Fig. 5.

also Paltridge and Platt, 1976). In the other extreme, turbulence is strong and we expect positive curvature in association with formation of a well-mixed or nearly well-mixed boundary layer.

To examine the possible relationship between potential temperature structure and the relative importance of clear-air radiative cooling, Fig. 6 shows the scaled curvature γ as a function of the ratio of the radiative cooling rate $|\Delta F|/h_s$ to the turbulent cooling rate $|Q_0|/h_R$

$$r \equiv \frac{|\Delta F| h_R}{h_s |Q_0|}.$$

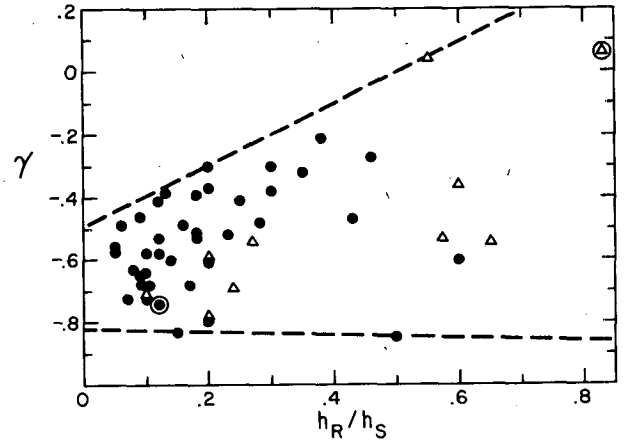

FIG. 7. Scaled curvature of the potential temperature profile γ, versus ratio of the depths of the turbulent-NBL and surface inversion h_R/h_s. Symbols as in Fig. 6.

Although the scatter is large, Fig. 6 shows a significant trend for the scaled curvature to become less negative with increasing ratio r. The least-squares regression model is

$$\gamma = -0.67 + 0.63\, r.$$

This result can be explained by recalling from Section 4 that night-to-night variations of the radiative flux divergence are small so that variations of the above ratio are dominated by variations in the turbulent flux divergence. The scaled curvature is large-negative when the surface heat flux is large and the depth of the turbulence is small. Small thickness of the turbulence layer relative to the inversion layer insures that the bulk of the inversion layer is dominated by clear-air radiative cooling. Strong surface heat flux implies strong cooling in the turbulent boundary layer which increases the temperature gradient in the lower part of the inversion layer, at least for cases where the turbulent layer is thin compared to the inversion layer. Strong stratification in the lower part of the inversion layer, in turn, corresponds to large curvature since the stratification is small at the top of the inversion layer.

Since the above arguments involve mainly the ratio of the depth of the turbulence to the inversion depth and since radiative and turbulent fluxes are not routinely calculated, we have plotted the scaled curvature against the ratio of depths h_R/h_s (Fig. 7). These two quantities require knowledge of only wind and temperature profiles. Fig. 7 shows a weak trend for

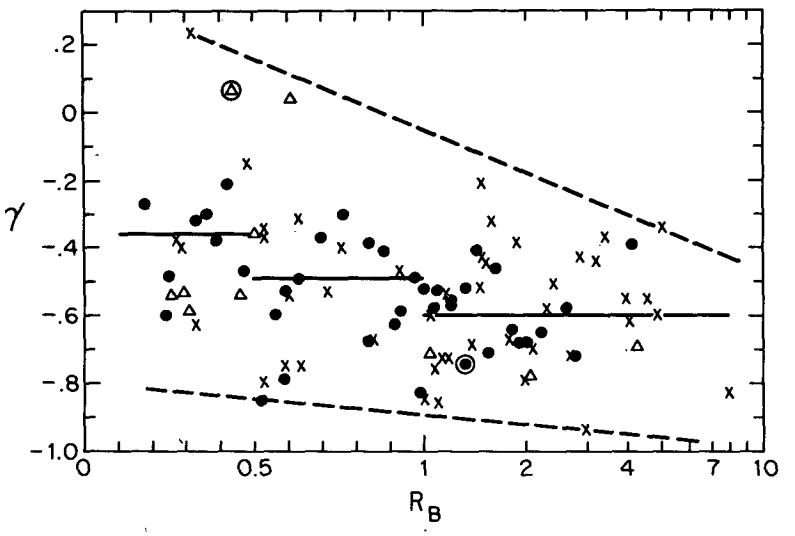

FIG. 8. Scaled curvature of the potential temperature profile γ, versus bulk Richardson number R_B. Symbols as in Fig. 6. Crosses indicate Koorin data.

the negative curvature to decrease as the depth of the turbulence increases and becomes closer to that of the inversion layer. The scatter is large, probably due partly to the fact that h_R/h_s is not uniquely related to the relative importance of the cooling rates due to turbulent and radiative fluxes. For example, the negative scaled curvature is expected to be small when the depth of the turbulence is relatively large in response to strong turbulent mixing. However, in the early evening, the turbulent boundary layer may not be thin compared to the still thin and developing inversion even though the turbulent heat flux is small. In agreement with this argument, the points in Fig. 7 with significant negative curvature and yet large values of the depth ratio occurred around or before 2100 LST.

We also expect the curvature to be related to the bulk Richardson number since increasing Richardson number usually implies decreasing turbulent activity. Here we define the bulk Richardson number R_B in terms of $V_{\max}$, the maximum wind speed within the layer instead of at the top of the layer. In this manner we do not seriously underestimate the shear when the wind maximum occurs within the inversion layer. Then

$$R_B \equiv \frac{g\Delta\theta/\theta_0}{V_{\max}^2} h_s ,$$

where $\Delta\theta$ is the change in potential temperature across the layer and θ_0 is the surface potential temperature.

Since this parameter R_B is easy to compute from only wind and temperature profiles, it is possible to easily extend this analysis to other data, such as the Koorin experiment (Clarke and Brook, 1979), for which missing information on humidity structure does not allow for more complete analysis. Here we include data for Koorin nights which satisfy the "clear-night" criteria discussed in Section 2. Fig. 8 shows that the relationship between scaled curvature and bulk Richardson number is rather weak for clear nights, although both the envelope of the points and the mean values inside each range of R_B values exhibit the expected trend. If we add the remaining Wangara nights, and thus include cloudy and/or windy situations, we find that for small bulk Richardson number the negative scaled curvature decreases rapidly and may even reverse to positive as the Richardson number decreases to still smaller values (Fig. 9). That is, for large bulk Richardson number normally occurring with weak winds and clear nights, the cooling of the inversion layer is mostly determined by clear-air radiation, which has no special relationship to the bulk Richardson number. This explains the weak trend and large scatter for Richardson numbers greater than one. However, if the bulk Richardson number of the inversion layer becomes sufficiently small, then turbulence exerts an important influence on the bulk temperature structure and the flow becomes more mixed with further decreases in the Richardson number. Models of the temperature structure of the stable boundary layer should qualitatively include this dependence of curvature on a bulk stability parameter such as the Richardson number.

The least-squares regression model for nondimensional curvature for Richardson numbers less than unity for the data in Fig. 9a is

$$\gamma = -0.14 - 0.6R_B. \qquad (5)$$

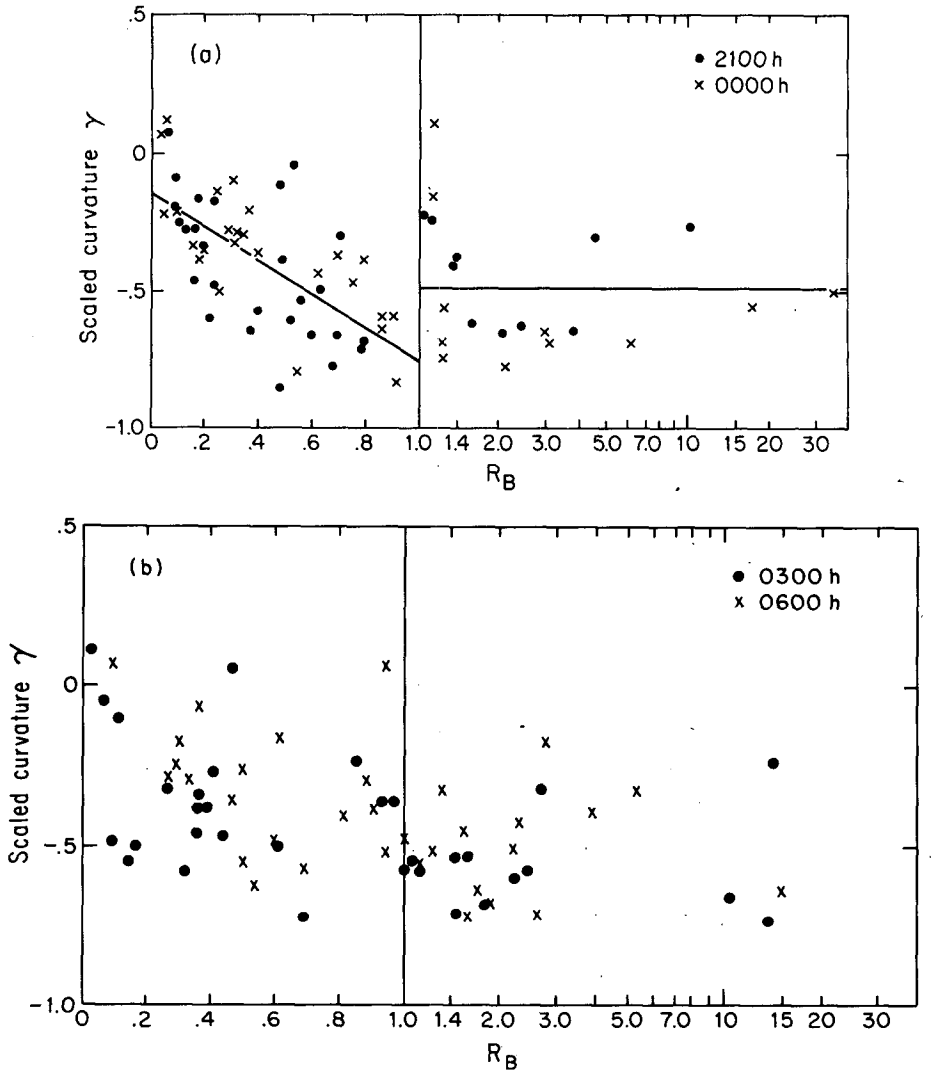

FIG. 9. Scaled curvature of the potential temperature profile γ, versus the bulk Richardson number R_B for Wangara profiles observed at (a) 2100 and 2400 LST and (b) 0300 and 0600 LST.

For Richardson numbers greater than unity the averaged value of the nondimensional curvature is −0.49. This relationship (5) can be used to simply approximate the thermodynamic structure from bulk properties of the nocturnal boundary layer. For comparison the cubic model of Yamada (1979),

$$\bar{\theta}(z) - \bar{\theta}(h_s) = -[\bar{\theta}(h_s) - \bar{\theta}(0)][1 - z/h_s]^3,$$

after finite differencing corresponds to $\gamma = -0.75$.

Also note that the relationship between scaled curvature and bulk Richardson number partially breaks down toward the end of the night (Fig. 9b). This latter period is normally associated with increasing stability and decreasing speed of the low-level jet and possible decay of the turbulence.

6. Conclusions and further discussion

For the data examined here, the turbulent heat flux divergence and clear-air radiative cooling, on the average, contribute about equally to the development of the nocturnal surface inversion. Cooling due to turbulence is confined to the lower part of the surface inversion layer. Clear-air radiative cooling extends the surface inversion to levels several times higher than the turbulent layer. The radiative cooling rate is a maximum near the inversion layer top, which not only acts to thicken further the inversion layer, but also reduces the stratification. Consequently, the surface inversion thickens throughout the night even though the depth of the turbulent layer does not show such a trend.

The stratification is weaker above the turbulence in the radiatively-cooled layer. This height-dependence of stratification corresponds to significant negative curvature of the profile of potential temperature. When the turbulence becomes strong enough to occupy most of the inversion layer, the negative curvature weakens and may even reverse to positive with the formation of a quasi-mixed layer.

For the data examined here, the importance of clear-air radiative cooling for the bulk of the boundary layer is relatively insensitive to the particular moisture structure and, as a result, varies from night to night much less than the turbulent surface heat flux. The crucial role of clear-air radiative cooling appears to preclude successful relation of the inversion depth to surface fluxes, as has been frequently attempted in the literature. This possibility may account for the fact that boundary-layer depth relationships based on surface fluxes explain less than 25% of the variance of the observed inversion depths (Yu, 1978). Mahrt *et al.* (1982) have recently reanalyzed these data by using the estimated depth of the turbulence instead of the inversion depth.

Since clear-air radiative cooling has not been successfully measured for the bulk of the surface inversion and since turbulent fluxes are weak and intermittent, future observational programs or analyses are likely to make only slow progress. Furthermore, nocturnal flow is strongly influenced by even weak slopes and surface inhomogeneity. Numerical modeling will therefore play a helpful and necessary role in future understanding of the nocturnal surface inversion. The results in this study suggest construction of a two-layer model of the nocturnal surface inversion, the lower layer dominated by turbulence, and the upper layer by clear-air radiative cooling. It is not certain if the inversion layer is significantly influenced by the overlying flow where the stratification is weak and occasional turbulence may occur.

Acknowledgments. The authors wish to thank J. J. Morcrette for helpful advice and for making available the results of his radiative computations, and P. Bougeault for helpful comments. Thanks are also due to L. Musson-Genon and R. C. Heald for computational assistance and to the reviewers for their many helpful, detailed comments.

This material is based upon work supported by the National Science Foundation under Grant No. ATM-7908308 and Direction de la Météorologie, Paris.

APPENDIX

The Radiative Calculation

The radiative calculation used in this study is quite similar to the one proposed by Sasamori (1972) and previously used by André *et al.* (1978) except that the ground emissivity ϵ is now taken into account. The vertical divergence of the longwave radiative flux $F(z)$ is computed according to

$$\frac{\partial F}{\partial z} = (1-\epsilon)\left\{B(0) - \int_0^\infty B(z')\frac{\partial A(0,z')}{\partial z'}\,dz'\right\} \times \frac{\partial A(0,z)}{\partial z} + \int_0^z \frac{\partial A(z',z)}{\partial z}\frac{\partial B}{\partial z'}\,dz' + \int_z^{z_T} \frac{\partial A(z,z')}{\partial z}\frac{\partial B}{\partial z'}\,dz' - \frac{\partial A(z,\infty)}{\partial z}B(z_T), \quad \text{(A1)}$$

where $B(z)$ is the blackbody emission at the mean temperature $T(z)$ at altitude z, and $A(z, z')$ is the total adsorptivity of water vapor and carbon dioxide between altitudes z and z'. z_T is the termination altitude of the vertical integration, above which the atmosphere is assumed isothermal, except at infinity where one assumes that $B(\infty)$ vanishes. This hypothesis allows for a simplified calculation of the downward flux $F\downarrow$ at level z_T [the last term in (A1)]. The fact that the underlying surface is not a perfect blackbody is taken into account through the emissivity correction described by the first term of the right-hand side of (A1). This correction represents the small difference between (a) heat loss due to the fact that the ground radiates less energy than a blackbody at the same temperature and (b) heat gain due to the fact that the ground also reflects part of the downward flux $F\downarrow$ reaching the surface (Kirchhoff's law).

Following Sasamori (1968) and Veyre *et al.* (1980), the total absorptivity $A(z, z')$ is expressed from the absorptivities due to water vapor in the rotation and vibration bands (A_{H_2O}), to water vapor dimer in the window region (A_{Dim}) and to carbon dioxide (A_{CO_2}) so that

$$A(z,z') = A_{H_2O}(u_{H_2O}) + A_{CO_2}(u_{CO_2})T_{15}(u_{H_2O}) + A_{Dim}(u_{Dim})T_w(u_{H_2O}). \quad \text{(A2)}$$

where u_{H_2O}, u_{Dim} and u_{CO_2} are, respectively, the corrected path lengths of water vapor, water vapor dimer and carbon dioxide between levels z and z':

$$u_{H_2O}(z,z') = \int_z^{z'} \bar{\rho}(\zeta)\bar{q}(\zeta)\left[\frac{\bar{p}(\zeta)}{p_0}\right]^{0.9}\left[\frac{T_0}{\bar{T}(\zeta)}\right]^{0.45} d\zeta, \quad \text{(A3)}$$

$$u_{CO_2}(z,z') = \int_z^{z'} \bar{\rho}(\zeta)q_c\left[\frac{\bar{p}(\zeta)}{p_0}\right]^{0.75} d\zeta, \quad \text{(A4)}$$

$$u_{Dim}(z,z') = \int_z^{z'} \bar{\rho}(\zeta)\bar{q}(\zeta)\bar{e}(\zeta) \times \exp\left\{1800\left(\frac{1}{\bar{T}(\zeta)} - \frac{1}{296}\right)\right\} d\zeta, \quad \text{(A5)}$$

where $\bar{\rho}$ and $\bar{p}$ are the standard density and pressure, $\bar{q}$ and $\bar{e}$ the mixing ratio and partial pressure of water vapor, $\bar{T}$ the temperature and q_c the mean concentration of carbon dioxide taken as 320 ppm throughout the whole atmosphere. In Eq. (A2), T_{15} and T_w are the transmissivities due to water vapor in the carbon dioxide band and in the window region, taken from Sasamori (1968) and Veyre *et al.* (1980) as

$$T_{15}(u_{H_2O}) = 1.33 - 0.832(u_{H_2O} + 0.0286)^{0.26}, \quad \text{(A6)}$$

and

$$T_w(u_{H_2O}) = \left(\sum_{i=0}^{4} a_i' u_{H_2O}^{\,i}\right)\Big/\left(\sum_{j=0}^{5} b_j' u_{H_2O}^{\,j}\right), \quad \text{(A7)}$$

while the absorptivities are chosen according to[3]

$$A_{H_2O}(u_{H_2O}) = \begin{cases} 0.846(3.59\ 10^{-5} + u_{H_2O})^{0.243} - 0.069 & \text{for } u_{H_2O} < 0.01 \text{ g cm}^{-2} \\ 0.24 \log_{10}(0.01 + u_{H_2O}) + 0.622 & \text{for } u_{H_2O} \geq 0.01 \text{ g cm}^{-2} \end{cases} \quad \text{(A8)}$$

$$A_{CO_2}(u_{CO_2}) = \begin{cases} 0.0676(0.01022 + u_{CO_2})^{0.421} - 0.00982 & \text{for } u_{CO_2} \leq 1 \text{ cm NTP} \\ 0.0546 \log_{10}(u_{CO_2}) + 0.0581 & \text{for } u_{CO_2} > 1 \text{ cm NTP} \end{cases} \quad \text{(A9)}$$

$$A_{Dim}(u_{Dim}) = \begin{cases} 0.4614\left[1 - \left(\sum_{i=0}^{2} a_i u_{Dim}^{\,i}\right)\Big/\left(\sum_{j=0}^{3} b_j u_{Dim}^{\,j}\right)\right] & \text{for } u_{Dim} \leq 0.5 \text{ atm g cm}^{-2} \\ 0.4614 & \text{for } u_{Dim} > 0.5 \text{ atm g cm}^{-2} \end{cases} \quad \text{(A10)}$$

In Eqs. (A7) and (A10) the constants a_i, b_j, a_i', b_j' are given by[3]

$$\left.\begin{aligned} &a_0 = 0.015075, \quad a_1 = -0.036185, \quad a_2 = 0.019245 \\ &b_0 = a_0, \quad b_1 = 0.19547, \quad b_2 = 0.75271, \quad b_3 = 1 \\ &a_0' = 7.76192\ 10^{-7}, \quad a_1' = 1.33836\ 10^{-3}, \quad a_2' = 0.166649, \quad a_3' = 2.17686, \quad a_4' = 2.6902 \\ &b_0' = 7.79097\ 10^{-7}, \quad b_1' = 1.36832\ 10^{-3}, \quad b_2' = 0.179601, \quad b_3' = 2.70573, \quad b_4' = 5.15119 \\ &b_5' = 1 \end{aligned}\right\} . \quad \text{(A11)}$$

Cooling profiles have been computed from the above model for various specified temperature and humidity profiles and compared with those from a much more elaborate radiative model employing as many as 68 spectral intervals in the infrared region above 4.5 μm (Morcrette, 1977). A typical result of the comparison is shown in Fig. A1, for the case of Wangara Day 34 at 0019L, for which the inversion was fairly strong (0.1°C m^{-1}) and the humidity varied significantly with height in the lowest 100 m. It can be seen that the simplified model produces an approximately correct evaluation of the destabilizing effect in the lowest 100 m and of the stabilizing tendency throughout the rest of the inversion and up to 700 m. The simplified model also leads to quantitatively consistent estimates of the magnitude of the radiative cooling. However, larger discrepancy exists in the first 10 or 20 m, probably due to inadequate resolution of the vertical grid close to the surface. Fortunately, the errors in this thin layer do not seriously affect our conclusions which are based on vertically integrated budgets. That is, the height h_s is much larger ($h_s \approx 300$ m) than this thin layer with possible significant errors, while in the case of the turbulent layer ($h_R \approx 50$ m), the radiative contribution to the cooling is much smaller than its turbulent counterpart.

It should be noted that the absorptivity function A_{H_2O} of water vapor in the non-window region rapidly saturates due to its logarithmic dependency on the amount of water vapor [see Eq. (A9)]. This explains the small sensitivity of radiative cooling rates to the mixing ratio of water vapor as already reported in Section 4. This insensitivity occurs as long as humidity remains within a "moderate" range (e.g., between 1 and 10 g kg^{-1}). This can be seen by considering the simplified case with height-independent lapse rate and humidity and with ground emissivity equal to 1. Then Eq. (A1) can be written as

$$\frac{\partial F}{\partial z} \approx \int_0^z \frac{\partial A(z', z)}{\partial z}\, dz' + \int_z^\infty \frac{\partial A(z, z')}{\partial z}\, dz'. \quad \text{(A12)}$$

The assumption of constant humidity implies that the partial derivatives with respect to z are approximately opposite to those with respect to z' [see, e.g., Eq. (A3)]. Then Eq. (A12) becomes

$$\frac{\partial F}{\partial z} \sim A(0, z) - A(z, \infty) \quad \text{(A13)}$$

[3] There are two misprints in Veyre *et al.* (1980). The exponent in the absorptivity for carbon dioxide should read 0.421 instead of 0.241, while the constant b_3' should be 2.70573 instead of 2.79573.

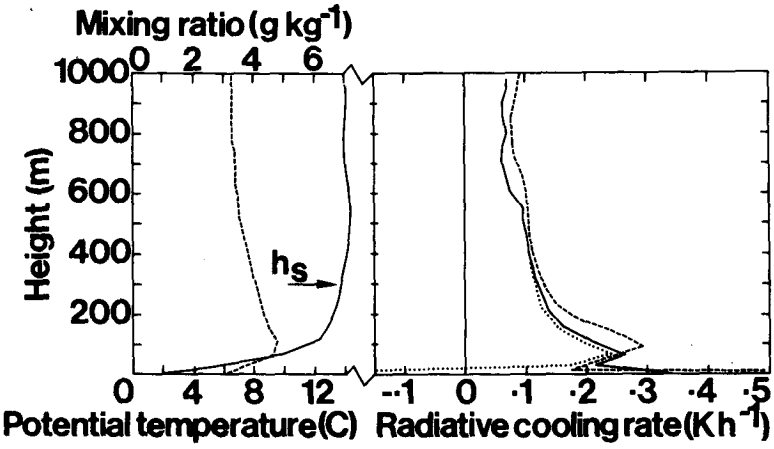

FIG. A1. Radiative cooling rates for Wangara Day 34 at 0019 LST. Left: potential temperature (solid line) and water-vapor mixing ratio (dashed line). Right: present model with $\epsilon = 0.965$ (solid line) and $\epsilon = 1$ (dotted line) and Morcrette's (1977) model with $\epsilon = 0.965$ (dashed line).

which does not exhibit large dependency on moisture as soon as z is large enough so that the water vapor content below level z almost saturates the absorptivity function. This argument does not apply if the mixing ratio for water vapor becomes so large that emission and absorption by water vapor dimer in the window region become important and contribute significantly to the radiative cooling (e.g. Grassl, 1974).

In the limit of vanishing humidity ($\bar{q} = 0$), the infrared fluxes are due only to carbon dioxide [see Eq. (A2)] and lead then to a vertical structure of the radiative cooling which is qualitatively similar throughout most of the inversion layer, but reduced by a factor of ~ 5, compared to cases with "moderate" humidity. All the above discussions are confirmed by the sensitivity experiments reported in Fig. 4, where a change of the moisture value from 1 to 10 gkg^{-1} leads to much smaller changes in the cooling rate compared to changes in the cooling rate resulting from variation of the thermodynamic structure between a strong surface inversion and a well-mixed state.

Based on Kondratyev (1969), the ground emissivity which appears in Eq. (A1) was chosen to be 0.965 for Wangara where the underlying surface was relatively dry with scarce vegetation and 0.98 for Voves where the surface was fairly wet and covered with nearly matured wheat. However, the radiative cooling profile is sensitive to the value of ground emissivity only close to the ground (see Fig. A1) as in Schaller (1977). Consequently, even a 1% error in the surface emissivity ϵ will not significantly influence the analysis.

It should finally be noticed that the present radiative model does not take into account the effects of possible aerosols, although these can be important in some conditions (Zdunkowski *et al.*, 1976; Paltridge and Platt, 1976). The aerosol content has not been measured for Wangara or Voves, but is believed to be low for both experiments since the surface was relatively moist and there were no obvious important local sources of aerosols.

REFERENCES

André, J. C., G. De Moor, P. Lacarrère, G. Therry and R. du Vachat, 1978: Modeling the 24 hour evolution of the mean and turbulent structures of the planetary boundary layer. *J. Atmos. Sci.*, **35**, 1861–1883.

——, and P. Lacarrère, 1980: Simulation détaillée de la couche limite atmosphérique. Comparaison avec la situation des 2 et 3 juillet 1977 à Voves. *La Météorologie VI*, **22**, 5–49.

Anfossi, D., P. Bacci and A. Longhetto, 1976: Forecasting of vertical temperature profiles in the atmosphere during nocturnal radiation inversions from air temperature trend at screen height. *Quart. J. Roy. Meteor. Soc.*, **102**, 173–180.

Ball, F. K., 1956: The theory of strong katabatic winds. *Aust. J. Phys.*, **9**, 373–386.

Brost, R. A., and J. C. Wyngaard, 1978: A model study of the stably-stratified planetary boundary layer. *J. Atmos. Sci.*, **35**, 1427–1440.

Brunt, D., 1934: *Physical and Dynamical Meteorology.* Cambridge University Press, 124–146.

Clarke, R. H., and R. R. Brook, 1979: *The Koorin Expedition—Atmospheric Boundary-Layer Data over Tropical Savannah Land.* Department of Science and the Environment, Australian Govt. Publ. Serv., Canberra, 359 pp.

——, A. J. Dyer, R. R. Brook, D. G. Reid and A. J. Troup, 1971: The Wangara experiment. Boundary-layer data, Pap. No. 19, Div. Meteor. Phys., CSIRO, Australia.

Coantic, M., and B. Seguin, 1971: On the interaction of turbulent and radiative transfers in the surface layer. *Bound.-Layer Meteor.*, **1**, 245–263.

Cole, A. E., A. Court and A. J. Kantor, 1965: Model Atmospheres. *Handbook of Geophysics and Space Environments.* McGraw-Hill, 2.1–2.22.

Delage, Y., 1974: A numerical study of the nocturnal atmospheric boundary layer. *Quart. J. Roy. Meteor. Soc.*, **100**, 351–364.

Elliott, W. P., 1964: The height variation of vertical heat flux near the ground. *Quart. J. Roy. Meteor. Soc.*, **90**, 260–265.

Funk, J. P., 1960: Measured radiative flux divergence near the ground at night. *Quart. J. Roy. Meteor. Soc.*, **86,** 382–389.

Grassl, H., 1974: Influence of different absorbers in the window region on radiative cooling (and on surface temperature determination). *Contrib. Atmos. Phys.*, **47,** 1–13.

Hicks, B. B., 1976: Wind profile relationships from the "Wangara" experiment. *Quart. J. Roy. Meteor. Soc.*, **102,** 535–551. Data catalog and additional report under preparation.

Klöppel, M., G. Stilke and C. Wamser, 1978: Experimental investigations into variations and comparisons with results of simple boundary-layer models. *Bound.-Layer Meteor.*, **15,** 135–146.

Kondo, J., 1971: Effect of radiative heat transfer on profiles of wind, temperature and water vapor in the atmosphere boundary layer. *J. Meteor. Soc. Japan,* **49,** 75–94.

Kondratyev, K. Ya., 1969: *Radiation in the Atmosphere.* Academic Press, 912 pp.

Mahrt, L., 1981: Modelling the depth of the stable boundary layer. *Bound.-Layer Meteor.*, **20,** 3–19.

——, R. C. Heald, D. H. Lenschow, B. Stankov and I. Troen, 1979: An observational study of the nocturnal boundary layer. *Bound.-Layer Meteor.*, **17,** 247–264.

——, J. C. André and R. C. Heald, 1982: On the depth of the nocturnal boundary layer. *J. Appl. Meteor.*, **21,** 96–98.

Melgarejo, J. W., and J. W. Deardorff, 1974: Stability functions for the boundary-layer resistance laws based on observed boundary-layer heights. *J. Atmos. Sci.*, **31,** 1324–1333.

——, and ——, 1975: Revision to stability functions for the boundary-layer resistance laws based upon observed boundary-layer heights. *J. Atmos. Sci.*, **32,** 837–839.

Morcrette, J. J., 1977: Calcul des flux infrarouges et des taux de refroidissement radiatif en atmosphère nuageuse. Thesis, University of Lille, 123 pp.

Moulsley, T. J., D. N. Asimakopoulos, R. S. Cole, B. A. Crease and S. J. Caughey, 1981: Measurement of boundary layer structure parameter profiles by acoustic sounding and comparison with direct measurements. *Quart. J. Roy. Meteor. Soc.*, **107,** 203–230.

Nieuwstadt, F. T. M., 1980: A rate equation for the inversion height in a nocturnal boundary layer. *J. Appl. Meteor.*, **19,** 1445–1447.

Ottersten, H., R. Hardy, K. Little and C. Gordon, 1973: Radar and sodar probing of waves and turbulence in stratified stable clear layers. *Bound.-Layer Meteor.*, **4,** 47–89.

Paltridge, G. W., and C. M. R. Platt, 1976: *Radiation Processes in Meteorology and Climatology.* Elsevier, 318 pp.

Perrier, A., B. Itier, J. M. Bertolini and A. Blanco de Pablos, 1975: Mesure automatique du bilan d'énergie d'une culture; exemples d'application. *Ann. Agron.*, **26,** 19–40.

Sasamori, T., 1968: The radiative cooling calculations for application to general circulation experiments. *J. Appl. Meteor.* **7,** 721–729.

——, 1972: A linear harmonic analysis of atmospheric motion with radiative dissipation. *J. Meteor. Soc. Japan,* **50,** 505–517.

Schaller, E., 1977: Time and height variability of the sensible heat flux in the surface layer. *Bound.-Layer Meteor.*, **11,** 329–354.

Veyre, P., G. Sommeria, and Y. Fouquart, 1980: Modélisation de l'effet des hétérogénéités du champ radiatif infrarouge sur la dynamique des nuages. *J. Rech. Atmos.*, **14,** 89–108.

Webb, E. K., 1970: Profile relationships: The log-linear range and extension to strong stability. *Quart. J. Roy. Meteor. Soc.*, **96,** 67–90.

Wyngaard, J. C., 1975: Modeling the planetary boundary layer. Extension to the stable case. *Bound.-Layer Meteor.*, **9,** 441–460.

Yamada, T., 1979: Prediction of the nocturnal surface inversion height. *J. Appl. Meteor.*, **18,** 526–531.

Yu, T. W., 1978: Determining height of the nocturnal boundary layer. *J. Appl. Meteor.*, **17,** 28–33.

Zdunkowski, W. G., R. M. Welch and J. Paegle, 1976: One-dimensional numerical simulation of the effect of air pollution on the planetary boundary layer. *J. Atmos. Sci.*, **33,** 2399–2414.

Zeman, O., 1979: Parameterization of the dynamics of stable boundary-layer flow and nocturnal jets. *J. Atmos. Sci.*, **36,** 792–804.